AIP | Physics of Fluids

Pressure and partial wetting effects on superhydrophobic friction reduction in microchannel flow

Tae Jin Kim and Carlos Hidrovo

Citation: Phys. Fluids **24**, 112003 (2012); doi: 10.1063/1.4767469
View online: http://dx.doi.org/10.1063/1.4767469
View Table of Contents: http://pof.aip.org/resource/1/PHFLE6/v24/i11
Published by the American Institute of Physics.

Pressure and partial wetting effects on superhydrophobic friction reduction in microchannel flow

Tae Jin Kim[a] and Carlos Hidrovo[b]
Department of Mechanical Engineering, The University of Texas at Austin, Austin, Texas 78712, USA

(Received 22 January 2012; accepted 10 September 2012; published online 26 November 2012)

Friction reduction in microchannel flows can help alleviate the inherently taxing pumping power requirements associated with the dimensions involved. One possible way of achieving friction reduction is through the introduction of surface microtexturing that can lead to a superhydrophobic Cassie-Baxter state. The Cassie-Baxter state is characterized by the presence of air pockets within the surface microtexturing believed to act as an effective "shear free" (or at least shear reduced) layer, decreasing the overall friction characteristics of the surface. Most work in this area has concentrated on optimizing the surface microtexturing geometry to maximize the friction reduction effects and overall stability of the Cassie-Baxter state. However, less attention has been paid to the effects of partially wetted conditions induced by pressure and the correlation between the liquid-gas interface location within the surface microtexturing and the microchannel flow characteristics. This is mainly attributed to the difficulty in tracking the interface shape and location within the microtexturing in the typical top-down view arrangements used in most studies. In this paper, a rectangular microchannel with regular microtexturing on the sidewalls is used to visualize and track the location of the air-water interface within the roughness elements. While visually tracking the wetting conditions in the microtextures, pressure drops versus flow rates for each microchannel are measured and analyzed in terms of the non-dimensional friction coefficient. The frictional behavior of the Poiseuille flow suggests that (1) the air-water interface more closely resembles a no-slip boundary rather than a shear-free one, (2) the friction is rather insensitive to the degree of microtexturing wetting, and (3) the fully wetted (Wenzel state) microtexturing provides lower friction than the non-wetted one (Cassie state), in corroboration with observations (1) and (2).
 [http://dx.doi.org/10.1063/1.4767469]

I. INTRODUCTION

Duct flow is ubiquitous in engineering applications ranging in scale from plumbing networks to miniaturized drug delivery systems. The conventional wisdom in duct flow is that a no-slip boundary condition applies at the walls. However, duct flow pumping power requirements are reduced if the no-slip boundary condition is replaced by a slip boundary condition through surface modifications. With the advent of microsystems, a slip boundary condition can be achieved through the introduction of surface modifications and the aid of surface tension. Such surfaces are said to be under a superhydrophobic state, a surface with static contact angle greater than 150°. A sliding angle less than 5° (Refs. 1 and 2) can be achieved by microtexturing low energy surfaces, embedding an air layer underneath the liquid layer and hence lowering the contact angle hysteresis. This is termed the Cassie-Baxter state[3] and has drawn much attention due to its water-repelling characteristics[4,5] and drag/friction reduction possibilities with relatively simple surface modifications.

[a]Electronic mail: tj_kim@utexas.edu.
[b]Author to whom correspondence should be addressed. Electronic mail: hidrovo@mail.utexas.edu.

The primary objective of most work in this area has been geared towards optimizing the surface microgeometry to obtain the largest possible slip length and minimize pumping power requirements in microfluidic systems. It has been shown that the slip length is greater if the air pockets within the roughness elements are not isolated but rather connected throughout the texturing.[6,7] The approaches used to maximize the slip length include modifying the roughness element shape,[8,9] decreasing the roughness element size to the nano-scale,[10,11] and increasing the liquid-gas fraction.[12]

To understand the slip flow regime in these surfaces, different methodologies have been used to analyze the flow physics. Analytically and numerically, the slip length over various types of roughness configurations have been predicted by assuming a no-slip boundary condition at the solid wall and shear-free boundary condition at the liquid-gas interface.[13–16] Experimentally, photobleaching velocimetry has been used to measure the velocity at the wall,[17] micro-particle image velocimetry (μ-PIV) has been performed to map the velocity profile close to and within the surface roughness elements,[18–20] and pressure drops were measured to indirectly compare the friction reduction rate between a reduced-shear surface and a flat surface.[21]

Another area of interest in the study of superhydrophobic surfaces has been the prevention of the liquid layer from flooding the gas layer. Methods used to prevent liquid flooding include introducing air between the cavities,[22] roughening up the surface texturing with nano-cavities,[23,24] and chemically coating an already rough surface with a low surface energy material.[18,25] Prevention of liquid flooding has been extensively studied because once the cavities are fully wetted, termed as the Wenzel state,[26] it is difficult to transition back to the Cassie-Baxter state.[12] A large number of studies have focused on artificially restoring the Cassie-Baxter state, rather than preventing collapse of the water layer into the air layer, by utilizing electrolysis,[27] gas injection[28] or boiling of the flooded liquid layer.[29] While various approaches have been made to maximize slip, maintain the Cassie-Baxter state, and measure friction reduction effects, the effects of the partially wetting microtextures on slip flows have received less attention and require careful consideration.

Toward this end, this paper will focus on the stability of the Cassie-Baxter state under pressure driven flow conditions and the effects that partial and complete roughness wetting (penetration of the gas-liquid interface into the microtexture gaps) have on the friction reduction characteristics. To properly visualize the gas-liquid interface and monitor its degree of penetration into the microtexturing, microchannels with an array of isolated trenches on the side were designed and fabricated. Global flow friction characteristics obtained from pressure versus flow rate measurements were correlated against micro-trench wetting conditions collected from this visualization setup. The experimental results for this particular enclosed microgeometry suggest that (1) the frictional characteristics of the air-water interface more closely resembles a no-slip condition rather than a shear-free behavior possibly due to immobilization of the air-water interface by contamination and/or constraining nature of the microgeometry, (2) the friction reduction is rather insensitive to liquid penetration into the roughness elements, at least for the geometries tested here and, related to these two previous corollaries, and (3) fully wetted Wenzel state micro-trenches provide better friction reduction than de-wetted, air filled Cassie state micro-trenches. It should be noted that while the notion and application of partial two-phase flow in superhydrophobic surfaces for friction reduction has been recently extended to external and turbulent flows,[30–32] the conclusions drawn from this paper strictly pertain to microchannel flows in the laminar regime.

II. BACKGROUND

A. Superhydrophobic states

The study of superhydrophobic surfaces has been inspired by the self-cleaning capabilities of a lotus leaf,[33] with the two major classifications of this phenomenon being pioneered by Wenzel and Cassie/Baxter.[34] The Wenzel state of a superhydrophobic surface entails complete interstitial wetting of the solid roughness elements underneath a liquid droplet, pinning it to the solid substrate. The microscopic and macroscopic contact angles are related by the Wenzel equation,

$$\cos\theta_W = r\cos\theta_Y, \tag{1}$$

where θ_Y is the Young's contact angle and r is the roughness factor, the ratio between the actual surface area to the nominal macroscopic area. Since the Wenzel state results in pinning of the droplet, experiments have indicated that fluid flow over such surfaces will reduce to a no-slip boundary condition[10] or even increased friction/drag conditions.[35]

On the other hand, the Cassie-Baxter state is a superhydrophobic state where the microscopic cavities are filled with gas or a different liquid underneath the liquid droplet. The Cassie-Baxter equation relating microscopic and macroscopic contact angle of a rough surface is given by

$$\cos\theta_{CB} = \phi_S \cos\theta_Y - (1 - \phi_S), \tag{2}$$

where ϕ_S is the solid fraction ratio between the actual wetted area of the solid and the nominal area. It is a common understanding that this effect leads to a reduction in drag/friction for fluid flow over solid surfaces and has been extensively studied.[6,21,36]

B. Friction reduction characterization

While studies have shown that slip can be achieved on smooth hydrophobic surfaces as well,[37,38] a consensus exists that a finite but larger slip velocity can be achieved if there are pockets of air in the surface. When performing analytical and numerical simulations on this type of slip flow,[14–16,39] the effective slip is calculated by assuming a no-slip boundary condition in the land region (solid-liquid interface) and a shear-free boundary condition in the gap region (liquid-gas interface). However, actual flow over microtextured surface involves various wetting conditions, where the microtextures are de-wetting, partially wetting, or fully wetting.

The appropriate metric to compare frictional characteristics for laminar duct flow with different microtexture configurations is the Darcy friction factor – Reynolds number product (*fRe*). The *fRe* for an internal laminar flow is given by

$$fRe = \frac{2\Delta P \cdot A D_h^2}{\mu Q L}, \tag{3}$$

where ΔP is the pressure drop from the inlet to the outlet, A is the nominal cross-sectional area of the land section, D_h is the nominal hydraulic diameter of the land section, μ is the averaged fluid (water) viscosity, Q is the measured flow rate, and L is the total length of the micro-trenched section in the microchannel. The *fRe* can also be interpreted as the non-dimensional hydraulic resistance, R_h, where $R_h = \Delta P / Q$ and therefore $fRe = R_h \cdot 2AD_h^2 / \mu L$. For the analysis presented here, the cross-sectional dimension in the land regions (see Sec. III A for specific geometry) has been selected as the global parameter in order to directly compare the dimensionless friction factors between different micro-trench configurations. This is justifiable since the purpose of this work is to assess the effect of microtexturing wetting on the friction reduction effects, and as such the micro-trenches are not considered part of the main flow section but rather surface features. The same logic is applied when calculating *Re* values. In this paper, we investigate the effective friction reduction effects of laminar flow over microtextures with isolated gaps depending on the wetting degree of the microtextures.

III. EXPERIMENTAL SETUP AND METHODOLOGY

A. Side trenched microchannels fabrication

In order to accurately track the wetting criteria of the artificial surface roughness, the microtextures are designed as isolated micro-trenches on the side walls oriented transverse to the water flow (Fig. 1). With this design, the air-water interface in individual micro-trenches can be efficiently visualized. Byun *et al.*[40] used a similar design to observe the wetting transition between de-wetted and fully wetted states and measured the slip lengths at the wall. However, their microchannel cross-sectional geometries were different for different wetting criteria experiments, the viscous losses from the top and bottom walls were dominant since the microchannel depths (where the microtexturing resides) were significantly smaller that their widths (~1:10 aspect ratio), and the slip lengths were

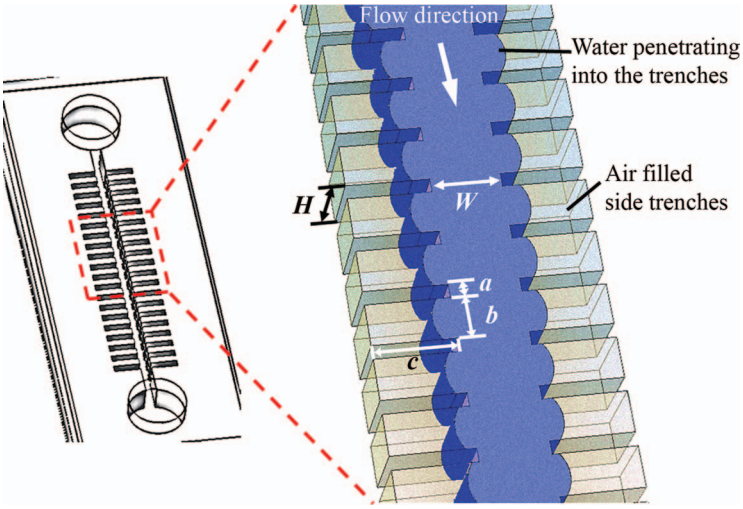

FIG. 1. A 3D schematic view of a side trenched microchannel with liquid penetrating into the air cavities. More penetration is to be expected upstream of the microchannel than downstream since the pressure is higher.

measured for the de-wetted state only. To our knowledge, the study presented in the current paper is the first attempt to experimentally quantify the partial wetting effects on microchannel friction using a consistent cross-sectional geometry of larger aspect ratio (~1:1) with significant friction reduction effects from the superhydrophobic surfaces.

A bare silicon wafer was spin coated with Su-8 2050 negative photoresist (Microchem) where the replicating mold for the PDMS (polydimethylsiloxane) microfluidic channels layouts were created through a photolithographic procedure. The wafer was then silanized (UCT specialties, LLC) for at least an hour in a vacuum desiccator to fluorinate the Su-8 replicating mold. A PDMS base and solvent (Dow Corning) mixture, with a volume ratio of 10:1, was poured onto the mold and cured at 80 °C for 2 h. The cured PDMS with microfeatures was then peeled off the mold and sliced into individual slabs. A complimentary set of PDMS slabs without microfeatures were fabricated and bonded to the featured PDMS slabs using an oxygen plasma cleaner (Harrick Plasma) at 29 Watts for 20 s to create the enclosed microchannels. Once the bonding was complete, the samples were baked overnight at 80 °C. Due to the nature of photolithography and the replicating process,[41,42] the channels have a trapezoidal cross-section rather than a rectangular one.

Prior to conducting tests, the microchannel samples dimensions (Table I) were measured through optical microscopy ($M = 40\times$, $NA = 0.60$). Careful measurement of the actual microchannel

TABLE I. Mean measured dimensions of the PDMS microchannel for each micro-trench configuration (N = 5) and the uncertainty due to instrument and measurement errors. Measurements were taken at different locations along the length of each microchannel sample. The land ($a = 15$ μm and $a = 55$ μm) represents the nominal distance between one edge to the other.

	W_{bottom}		W_{top}		H	
Trench dimension (μm)	Mean (μm)	Uncert. (μm)	Mean (μm)	Uncert. (μm)	Mean (μm)	Uncert. (μm)
Baseline	94.2	1.4	106.3	0.5	125.3	2.1
$a = 15, b = 65$ $c = 30$	103.7	1.3	105.3	0.8	124.7	2.0
$a = 15, b = 65, c = 60$	106.6	1.6	104.5	0.5	124.9	2.0
$a = 15, b = 65, c = 120$	111.6	2.4	103.9	0.5	123.8	2.0
$a = 15, b = 65, c = 230$	110.5	2.9	104.5	0.4	123.8	1.9
$a = 55, b = 65, c = 30$	95.5	0.7	106.8	0.8	124.3	2.0
$a = 55, b = 65, c = 60$	95.9	1.2	106.7	0.6	123.1	2.4
$a = 55, b = 65, c = 120$	96.4	1.0	106.1	0.5	121.1	2.2
$a = 55, b = 65, c = 230$	95.9	1.0	106.3	0.7	120.3	2.3

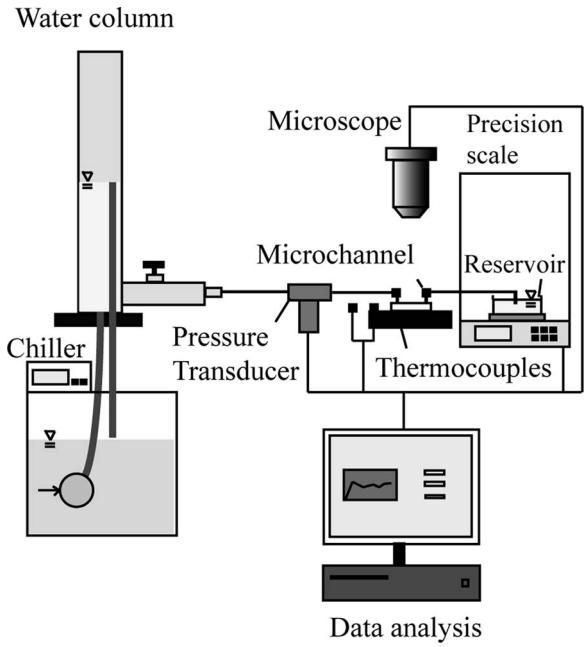

FIG. 2. Schematic diagram of the experimental setup. Pressure drop, flow rate and temperature are measured during a microchannel sample experiment. The experiments were repeated 5–6 times for each micro-trench configurations, and newly fabricated PDMS microchannels were used for each trial. By using a new microchannel for each trial, contamination issues are minimized.

dimensions are required[43] since the friction analysis is quite sensitive to the channel geometry and dimensions.

B. Pressure – flow rate measuring system

A constant head pressure setup and a differential mass measurement system (Fig. 2) are used to assess the frictional characteristics of the microchannel samples. A water reservoir with a controllable column height is used to generate the constant pressure source for flow into the microchannels. A liquid pump is used to constantly feed water to the reservoir while a draining pipe in the reservoir controlled the height of the water column. In order to maintain the water temperature as constant as possible, the liquid pump is submerged in a chiller set at room temperature.

By controlling the column height, the differential pressure supplied to the microfluidic channel inlet ranged from 800 Pa to 6000 Pa at increments of 400 Pa. The pressure drop was measured by connecting a differential pressure transducer (PX409, Omega) near the inlet and outlet of the microchannel. Since the differential pressure transducer was connected between the microchannel inlet and outlet ports, most of the pressure drop measured was due to losses within the microchannel. Also, in order to prevent the air in the left and right trenches from merging together due to the de-wetting characteristics of PDMS, the minimum absolute pressure of the system was increased above atmospheric conditions by placing the water collection reservoir approximately 10 cm above the PDMS microchannel exit. An example of the merging air layers if the microchannel experiences vacuum pressure conditions is shown in Fig. 3. The inlet of the microchannel is connected to a water reservoir at atmospheric pressure and the outlet is connected to a vacuum line, and a differential pressure of 6000 Pa is applied. While this is an extreme case, the figure suggests that the pressure of the water flow should be under positive gage pressure throughout the microchannel, thus requiring the collection reservoir to be placed above the microchannel.

Flow rate measurements were performed by collecting and weighting the water outflow from the microchannels over time. The outlet tube was submerged in a smaller reservoir placed on a precision balance (GH-252, A&D Weighing). The flow rate was calculated by tracking the mass of

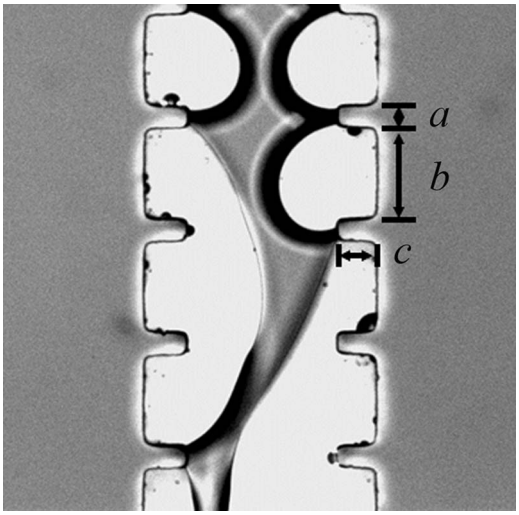

FIG. 3. Microscopic picture ($M = 10\times$, $NA = 0.3$) of a trenched microchannel ($a = 15$ μm, $b = 65$ μm, $c = 30$ μm) at approximately 90% from the upstream. The outlet is connected to a vacuum line and the differential pressure was maintained at 6000 Pa.

the water dispensed to the reservoir on the precision balance and the time taken to accumulate a given mass. Since the water reservoir is exposed to the environment, the evaporation rate from the reservoir was accounted for in each of the flow rate data. With the differential pressure and flow rate data, the friction in the microchannel can then be calculated.

However, as indicated by Lauga and Stone,[14] changes in viscosity may lead to confusion when measuring friction reduction effects in microchannel flow. Since the water viscosity decreases 2∼3% with a temperature increase of 1 °C monitoring the water temperature was necessary. Thermocouples were placed at the inlet and outlet tubes to measure the water temperature, and the changes in viscosity were assessed for each experiment. The averaged viscosities for each of the trials were then applied to the friction factor data.

C. Air-water interface visualization

Pressure versus flow rate measurements were complemented with visualization of the air-water interface location within the micro-trenches throughout the microchannel extent (Fig. 4). This visualization was performed with an upright microscope (LV100D-U, Nikon) connected to a scientific charge-coupled device camera (CoolSnap HQ, Photometrics). Each image covered 3.5% of the full extent of the microchannel length (18.5 mm), and was taken at 12 marked locations evenly spaced at 1.65 mm from the microchannel upstream location (inlet) to its downstream location (outlet).

The air-water interface visualization data was primarily used to establish whether a side micro-trench had been wetted, and if so, to quantify the degree of wetting (penetration). If the air-water interface was located at the edge or at the round vertex of the micro-trench base, the microchannel was considered non-wetted. On the other hand, if the interface traveled into the micro-trench gap and resided between the straight walls, the microchannel was considered wetted. Once the air-water interface had invaded the trench, the penetrated distance was measured to evaluate the partial wetting effects on the microchannel friction. The air-water interface visualization data was also used to address the pinching effects associated with the interface bowing outwards into the main microchannel section, an occurrence that would normally happen under lower inlet pressure conditions. This pinching effect has a flow cross sectional area reduction effect that would impact the measured friction as described later on.

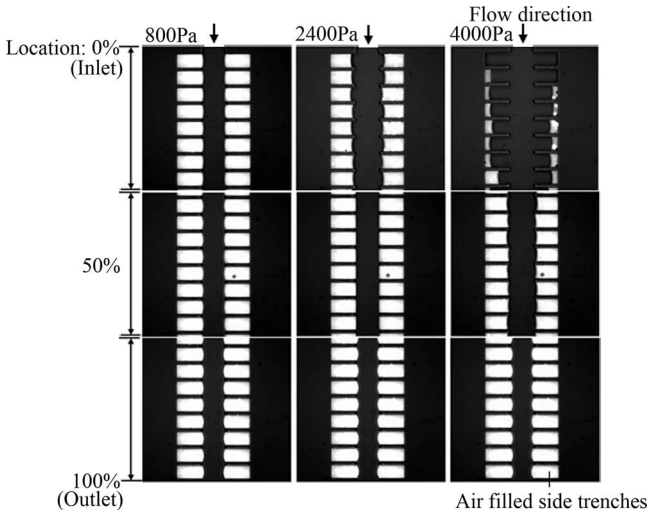

FIG. 4. Microscopic images ($M = 10\times$, $NA = 0.3$) of a micro-trenched microchannel ($a = 15$ μm, $b = 65$ μm, $c = 120$ μm) subject to different differential pressures. By observation, pressure is the largest near the inlet where water penetration is the deepest.

D. Effective flow width measurement for numerical *fRe* extremes

Two numerical extremes (COMSOL) of the *fRe* can be established by taking into account the varying cross-sectional flow area in the micro-trench gap section and modeling the air-water interface as either (1) a solid wall or (2) a perfect shear-free layer. To calculate the two numerical limits, information on the comprehensive hydraulic resistance value ($R_h = \Delta P/Q$) is required. The R_h can be acquired by first simulating the local fluidic resistance of individual micro-trenches based on the measured effective flow width w_{eff} data, and then summing all the local resistances in series to a single value.

The w_{eff} was measured by averaging the distance between the two air-water interfaces, where two pairs of trenches were selected over 12 equally spaced locations from the microchannel upstream to downstream regions. In order to imitate the flow conditions, the curvature of the air-water interfaces and the round micro-trench edges were measured and implemented in the numerical model. For each w_{eff} data, periodic trenches with the same w_{eff} were modeled until the flow was globally fully-developed (though locally the flow is constantly developing), and the corresponding resistance was measured. The flow is assumed as globally fully-developed since it was observed that the w_{eff} changes smoothly over the extent of the microchannel. The individual resistances were then compiled and the total resistance for the entire microchannel was obtained for each *Re*.

It should be noted that a no-slip boundary condition is assumed at the land section (non-trenched region) despite recent findings that some slip occurs in hydrophobic walls.[19,37,44] The slip length is in the nanometer scale, much smaller than the microchannel dimension, and hence slip effects on the solid wall can be neglected in this region despite the hydrophobic nature of PDMS. Moreover, while Bizonne *et al.*[45] indicated that the frictional characteristics may be affected if there are patches of air trapped in the solid land regions, the numerical results in this paper assume that the land regions are free of air. This was confirmed through the microscopy visualization.

IV. RESULTS

A. Experimental characterization of the global microchannel friction

In order to characterize and compare the partial wetting effects on microchannel friction, global frictional data, in the form of pressure drops versus flow rates, was acquired over a range of Reynolds number conditions.

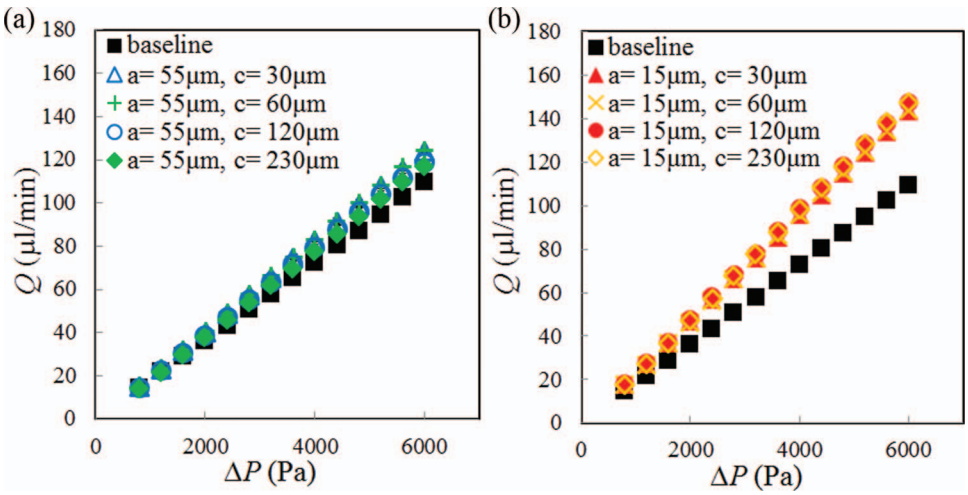

FIG. 5. Flow rate versus differential pressure for microchannels with (a) $a = 55\ \mu$m, $b = 65\ \mu$m (blue and green online) and (b) $a = 15\ \mu$m, $b = 65\ \mu$m (yellow and red online) for $c = 30\ \mu$m, 60 μm, 120 μm, and 230 μm. The baseline plot is for a microchannel with no trenches on the side walls, and the error bars represent the standard deviation of 5 to 6 repeated experiments.

Figure 5 depicts the flow rate versus ΔP for each microchannel configuration, where the baseline experiment is the microchannel without any trenches on the side walls. In Fig. 5, the flow rate of the microchannels with the smaller solid fraction ($\phi_S = a/(a+b) = 0.19$) increases with pressure at a higher rate than the ones with the larger solid fraction ($\phi_S = 0.45$). This result is not surprising as it is consistent with the conventional belief that smaller ϕ_S results in a larger effective slip.[12]

Since the actual ΔP is measured before/after the inlet/outlet, respectively, all the experimentally measured ΔP were adjusted by subtracting the numerically estimated ΔP from the converging inlet and the diverging outlet sections. By doing so, the *fRe* from Eq. (3) can be calculated based on the pressure drop in the micro-trenched section only. As observed in Fig. 6, the baseline data, based on the adjusted ΔP, agrees extremely well with the theoretical value line.

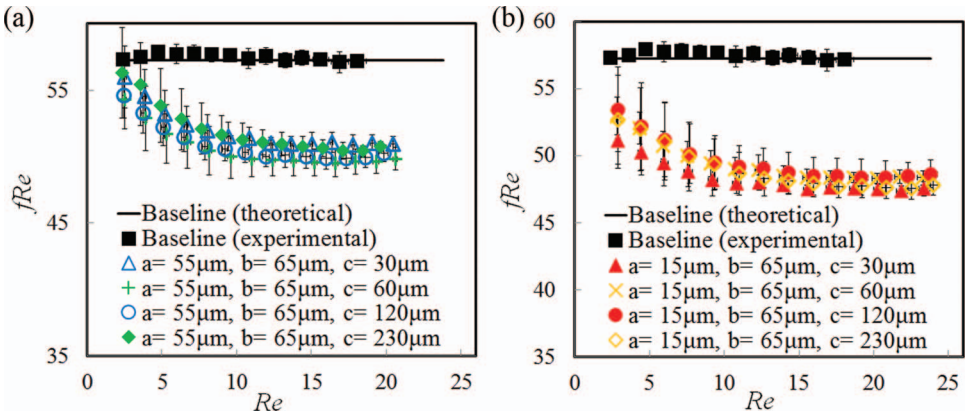

FIG. 6. Graph of *fRe* vs. *Re* for (a) $a = 55\ \mu$m and (b) $a = 15\ \mu$m, where the error bars represent the standard deviation among 5 to 6 similar samples (the error bars for *Re* are less than 5% and therefore obscured by the marker symbols). The theoretical *fRe* value for the baseline is ~ 57.2.[46] In the lower *Re*, *fRe* starts off at a larger value and then levels off approximately at $Re \sim 10$. The uncertainty due to the instrumental error specifications is less than 3.7% for *fRe* and 2.7% for *Re*. The uncertainty due to the measurement error is 1.8–6.4% for *fRe* and 1.3–6.1% for *Re*, which is consistent with the uncertainty from the standard deviation of the calculated *fRe* and *Re* values. The major and the minor losses from the external tubing are neglected since the combined losses account for 0.2–0.3% of the major loss in the microchannel.

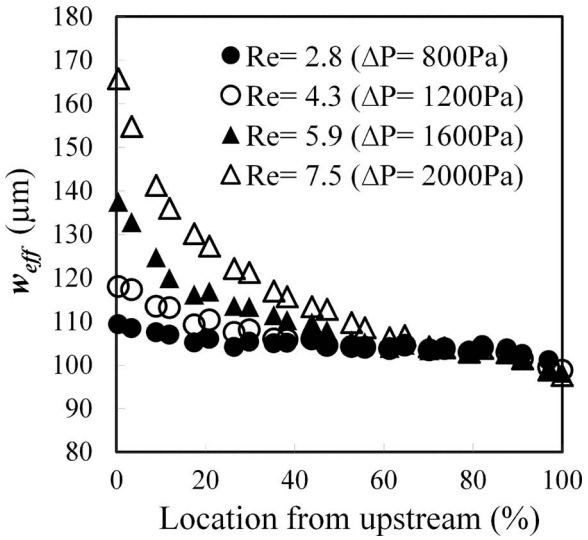

FIG. 7. Graph of w_{eff} vs. microchannel location. The w_{eff} data is measured for all the microchannels experimented and is applied to the numerical simulation. Since the microchannel height is constant, the change in w_{eff} represents the change in flow area ($a = 15\ \mu$m, $b = 65\ \mu$m, $c = 60\ \mu$m).

The *fRe* presented throughout the paper is calculated based on the nominal cross-section dimensions of the land sections, despite the fact that the flow cross-sectional area varied in the trench gap sections. It should be noted that the *Re* range varies with each microchannel configuration because the inlet pressure was controlled rather than the flow rate.

Several interesting features can be inferred from Fig. 6. In $Re < 10$ the *fRe* drops drastically with increasing *Re*, and in $10 < Re < 24$ the *fRe* becomes rather insensitive to *Re*. To understand the reasons behind these trends, the experimental data is compared with two extreme friction bounding limits obtained from numerical results.

B. Numerical simulation of upper and lower friction limits

As described in Sec. III D, the upper and lower numerical *fRe* extremes were calculated based on the w_{eff} measurements. Since the gage pressure decreases as the water travels downstream, the reduction in pressure leads to the de-wetting of the micro-trench cavities, especially at the outlet. According to the measured w_{eff} data (Fig. 7), the air-water interface protrudes into the micro-trench cavities near the microchannel outlet where the absolute pressure is the smallest.

The two numerical *fRe* limits are calculated by implementing the w_{eff} data and are compared with the experimental *fRe* value (trench dimensions of $a = 15\ \mu$m, $b = 65\ \mu$m, and $c = 60\ \mu$m). As expected, the experimental data falls in between the two numerical limits (Fig. 8). However, more interesting is that the experimental data trends more closely to the upper no-slip frictional bound, both in terms of *fRe* values and overall behavior with increasing *Re*. The *fRe* vs. *Re* graph behavior also suggests two major regions of interest – the lower *Re* region (2–10) where the *fRe* drops drastically with increasing *Re*, and the moderate *Re* region (10–25) where the *fRe* levels off and becomes insensitive to *Re*. These trends are consistent among all the different micro-trench configurations (Fig. 6), and will be discussed in more detail in Secs. IV C and IV D.

C. Friction (*fRe*) behavior in the lower Reynolds number region

In the lower *Re* region (<10), where a large portion of the micro-trenches are de-wetted, the friction increases with decreasing *Re*. This is also the behavior exhibited by the theoretical no-slip upper friction limit, which is markedly in contrast with the behavior of the shear-free lower friction limit, which increases with *Re*. The difference between the experimental *fRe* data and the numerical

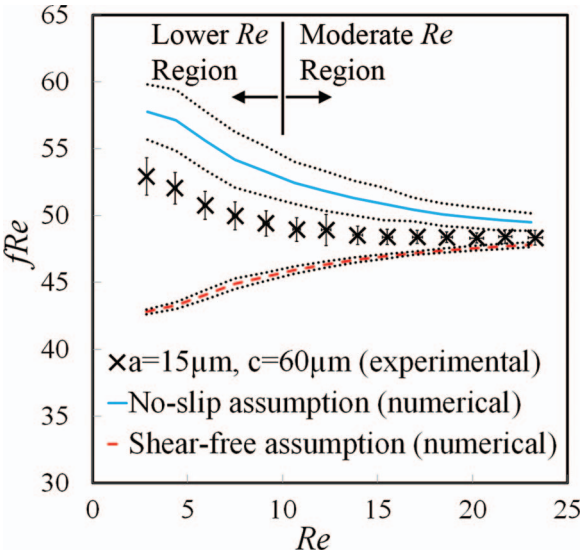

FIG. 8. Comprehensive *fRe* vs *Re* graph for experimental and numerical results for a trenched microchannel ($a = 15$ μm, $b = 65$ μm, $c = 60$ μm). The numerical results are based on the actual w_{eff} data, and the standard deviation of the results due to the fluctuations in water penetration from sample to sample are plotted as dotted lines above and below the averaged values. As expected, the experimental results are located between the two bounding numerical *fRe* limits (no-slip assumption and shear-free assumption at the air-water interface).

bounds are 7.4%–8.3% if the air-water interface is assumed as a solid wall (upper bound) and 8.8%–23.6% if the interface is assumed as a shear-free layer (lower bound).

Closer examination of the theoretical no-slip numerical results in this region reveals that the increase in hydrodynamic resistance with decreasing *Re* is the result of reduction in flow area due to pinching effects. This pinching results from de-wetting of the micro-trenches at the low pressure conditions. Since *Re* is proportional to the inlet pressure, a significant number of the micro-trenches are de-wetted in the lower *Re* region, leading to substantial pinching of the water flow throughout the extent of the microchannel. The lower *Re* the more severe this pinching is and the higher the friction is for a no-slip assumption (Fig. 9).

Contrastingly, the pinching effects for the shear-free case lead to a decrease in friction. Although pinching also results in an effective flow area reduction in this case, the viscous losses in this

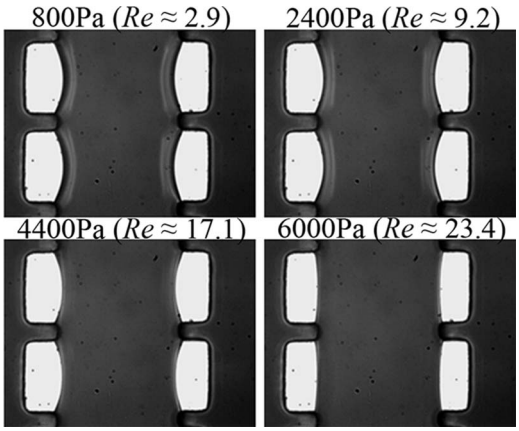

FIG. 9. Micrograph ($M = 40\times$, $NA = 0.60$) of pinching effects in a micro-trench section ($a = 15$ μm, $b = 65$ μm, $c = 30$ μm) located at 70% from upstream. It is observed that the air layer protrudes more into the water layer if the inlet pressure (and hence *Re*) is lower.

shear-free interface arrangement are primarily dominated by the water in contact with the non-textured surfaces at the top and bottom walls of the microchannel. Since there is no viscous dissipation at the left and right sides of the water layer in the micro-trench regions (where the air-water interface is located), the friction of the water layer will decrease if the microchannel is strongly de-wetted and water contact with the top/bottom walls is reduced. Only for extreme cases where the flow area is greatly reduced over de-wetted microtextures in this shear-free configuration would the friction increase with pinching.[47,48]

Although it has been traditional practice to treat the air-water interface as a perfect shear-free region in analytical and numerical models,[14,16,49] the behavior and values of the experimental frictional data presented here suggests that the air-water interface more closely resembles a no-slip boundary condition. Furthermore, microchannel friction is sensitive to even small reductions in the cross-sectional flow area for this same reason. One possible explanation why the air-water interface behaves closer to a solid wall may be due to contamination of the air-water interface, which could render it rather immobile. Studies have shown that even small contaminations of surfactants result in a solid wall-like behavior of the air-water interface, and it has been an extremely difficult process to maintain the system free of contamination.[50] Even with the use of distilled water, it is possible to incur interface contamination from the PDMS surface, external tubing and/or connectors.

D. Friction (*fRe*) behavior in the moderate Reynolds number region

In the moderate *Re* region (10–25), where a large portion of the micro-trenches have been penetrated and wetted by the air-water interface, the friction is rather insensitive to *Re*. Likewise, the upper and lower bound numerical limits converge close to the experimental data as *Re* increases.

To understand the significance of these observations, the wetting characteristics of the micro-trenches are explored first. In the moderate *Re* region, the inlet pressures are well above the capillary pressure required to maintain the non-wetting state. Wetting of the trenches generally starts at 1200 Pa inlet pressure, which corresponds to $Re = 4.3$–4.6 for $a = 15$ μm trenches and $Re = 3.6$–3.9 for $a = 55$ μm trenches (Fig. 10). In the figure, it should be noted that the wetting percentage does not necessarily mean that the trenches are fully wetted but can also be partially wetted: it merely indicates the percentage of trenches where the liquid layer has overcome the Laplace pressure.

It can be inferred from Fig. 10 that the global degree of wetting for the different micro-trench configurations does not seem to significantly affect the microchannel friction, as the fraction of

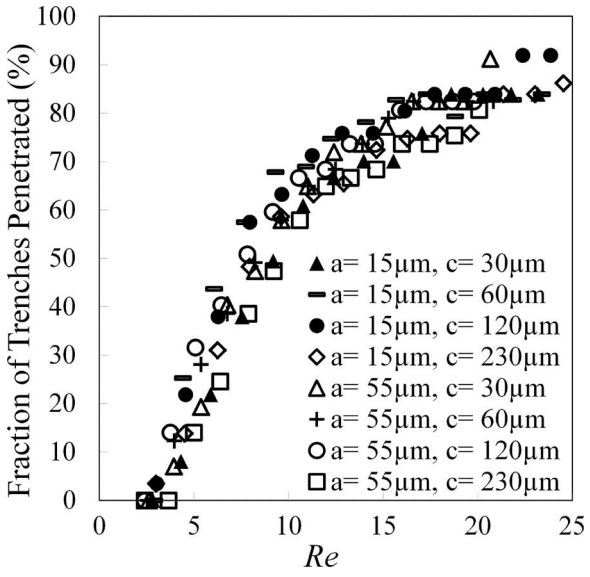

FIG. 10. Fraction of trenches penetrated vs. *Re* for a single microchannel sample (left side of the trenches only). In the higher *Re* (or ΔP) range, the wetting of the trenches no longer increases significantly.

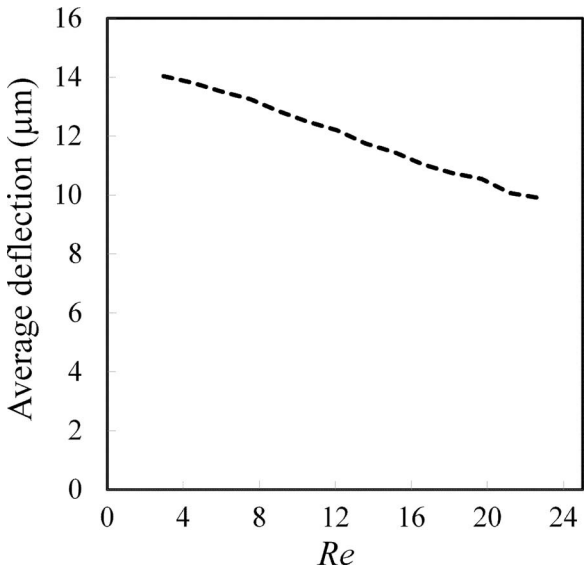

FIG. 11. Numerical results of the streamline deflection into a fully wet micro-trench element. The average deflection of the streamline is measured from the edge of the micro-trench land into the micro-trench gaps. As *Re* increases the streamline deflection into the micro-trench decreases.

penetrated trenches significantly increases from 50 to 85% over this moderate *Re* region. The insensitiveness of the microchannel friction to wetting effects is further revealed by tracking the magnitude of the water penetration into the micro-trenches. The shallowest micro-trench configuration demonstrates a binary behavior when transitioning from a non-wetting state to a fully-wetting state. As the micro-trench depth increases, the transition becomes progressively smoother. Nonetheless, the wetting behaviors of different micro-trench configurations do not seem to significantly affect the microchannel friction in the moderate *Re* region.

One possible explanation for the insensitiveness of the microchannel friction to *Re* (and degree of micro-trench wetting) in this region is the limitation on how much the streamlines can bend into the penetrated trenches since the flow is $Re > 1$. Unless the flow is in Stokes flow, the effective flow width should not significantly increase with pressure once the water layer penetrates beyond a certain distance into the trenches. The limitation on how much the streamline can deflect into the micro-trenches can be assessed from numerical simulations of a fully wetted micro-trench case (Fig. 11). The fully wetted case was selected since it provides the maximum penetration of water into the trenches and hence the maximum possible deflection of the streamlines into the trenches. In the figure, the magnitude of the deflection decreases with increasing *Re*, where the average deflection of the streamline into the micro-trench gaps ranges from 10–14 μm. The limitations on how much the streamlines can bend infers that the microchannel friction is less likely to be affected by *Re* (and hence ΔP) once the water penetrates beyond a certain distance into the micro-trenches. This also explains why the theoretical bound limits converge at higher *Re* values, which also correspond to higher micro-trench penetration (Fig. 8). Under these limited streamline penetration conditions, whether the air-water interface is no-slip or shear-free is irrelevant.

E. Comparison between fully-wetted and initially de-wetted micro-trenches

In order to further explore and validate the results presented before, experimental tests and numerical simulations for microchannels with fully wetted micro-trenches throughout the whole extent of *Re* were performed. The micro-trenches were pre-wetted by pressurizing the microchannels ($\sim$1.2 kPa) until all the micro-trenches were fully impregnated with water. Once the micro-trenches were fully wetted, the experiments were performed from $Re = 2.9$ ($\Delta P = 800$ Pa) to $Re = 22.1$ ($\Delta P = 6000$ Pa).

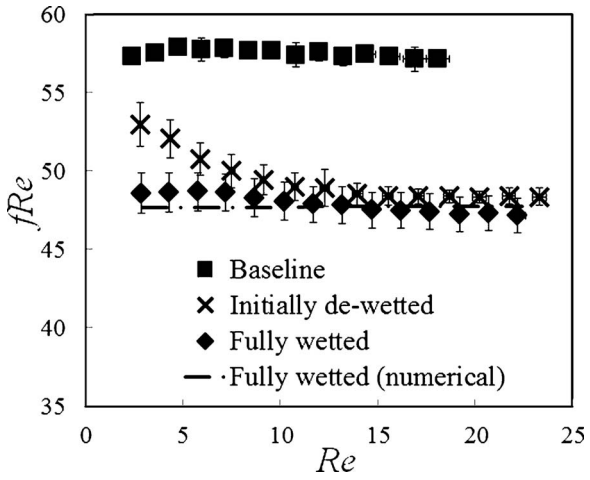

FIG. 12. Comparison of friction in a microchannel between Cassie-Baxter state and Wenzel state ($a = 15\ \mu$m, $b = 65\ \mu$m, $c = 60\ \mu$m). For the numerical *fRe* calculations, a rectangular cross-sectional area is assumed since the error in *fRe* due to the difference between the microchannel geometry measured in Table I and the rectangular cross-section is <0.5%.

Figure 12 shows a comparison of the *fRe* values for microchannels with initially air filled micro-trenches (Cassie-Baxter state), as presented in the sections before, and microchannels with pre-wetted micro-trenches (Wenzel state), alongside numerical simulations results for the latter. The experimental *fRe* for the fully-wetted microchannels are generally less sensitive to *Re*, whereas the initially de-wetted microchannels start at a considerably larger *fRe* values but then converge closely to the fully wetted micro-trenches values as the interface penetration becomes substantial above $Re \sim 7$. This suggests that for $Re < 7$, where the majority of the micro-trenches are classified as de-wetted, the pinching effects result in a larger friction than the fully wetted microchannels, corroborating the no-slip behavior of the interface. As mentioned before, surfactant contamination may immobilize the air-water interface leading to flow reduction (increased friction) when pinching occurs in the de-wetted microchannels. On the other hand, the water molecules can freely bend into the micro-trench gaps in the fully wetted microchannels, thus increasing the effective flow area. This increase in effective flow area leads to a larger friction reduction effect than the water flow over the immobile air-water interface. Nonetheless, it should be noted that substantial friction reduction can be achieved regardless of the wetting or de-wetting nature of the micro-trenches.

It should also be noted in Fig. 12 that the experimental *fRe* for the fully wetted case decreases approximately by 2.9% within the range $2.9 < Re < 23.6$, falling slightly below the numerical simulations towards the larger *Re* values. This is attributed to microchannel expansion effects associated with the increase in inlet pressure.[51] It was observed that the baseline microchannel width 20% downstream from the inlet expanded approximately 0.5% between $\Delta P = 800$ Pa and $\Delta P = 6000$ Pa. A corresponding expansion based on these baseline microchannel observations was included in the numerical simulations of the microchannel with fully wetted micro-trenches. Although a larger expansion can probably be expected for the micro-trenched sample (less bounding material) improving agreement between the experimental and numerical results at the larger *Re*, they do fall within the uncertainty of each other (error bars) throughout the whole *Re* range and are therefore validated.

V. CONCLUSIONS

Microtextured superhydrophobic surfaces have been extensively used to alleviate the taxing pumping power requirements of microchannel flow by reducing wall friction. The prevalent notion has been that friction reduction is achieved by inducing the Cassie-Baxter state, where the formation of air pockets leads to shear-free regions. However, to properly assess the role that the microgeometry and air pockets play in this phenomenon, it is important to understand the pressure and partial

wetting effects of the microtexturing on the friction reduction characteristics. Through differential pressure versus flow rate measurements and microscopic visualization of the interface location, three major observations on the frictional behavior were made in the *Re* range 2–25. These experimental observations were validated and complemented by COMSOL based numerical simulations of the upper (no-slip air-water interface) and lower (shear-free air-water interface) bounds friction limits for the flows.

In the lower *Re* region (2–10), the friction of the de-wetted microchannels increased with decreasing *Re*. Comparison of the $fRe_{experimental}$ with numerical results of $fRe_{effective,no\text{-}slip}$ and $fRe_{effective,no\text{-}slip}$, revealed that the frictional characteristics of the air-water interface were better approximated by a no-slip boundary condition than a shear-free one, as it is widely assumed. The friction is larger for de-wetted conditions, were the air-water interface seems to slightly protrude into the microchannel main section, pinching and reducing the effective flow area in the micro-trenches gap sections. The friction increase with water layer pinching in these sections is consistent with a no-slip boundary condition for the air-water interface. This behavior would be the result of a highly immobilized air-water interface. It is speculated that this immobilization results from either contamination (presence of particulates or surfactants, aggregating at the interface), a restraining geometry ("pinning" of the water molecules in tension at the interface, exacerbated by the short micro-trench gap span), or both. Either one of these possibilities has important implications in the actual implementation of the surfaces. If contamination is the major culprit, since distilled water was used in the experiments presented here, it is very likely that this mechanism would be more prevalent in actual, real life applications. On the other hand, immobilization due to a restraining microgeometry would pose a serious compromise between achieving a stable Cassie state and producing highly mobile interfaces, even for open microgeometries (i.e., micropillars) where feature separation is dictated by the Laplace capillary pressure. However, as would be argued later, this might not be as constraining an engineering compromise as posed here.

In the moderate *Re* region (10–25), the frictional characteristics of the microtextured microchannels were rather insensitive to the wetting degree (air-water interface penetration) of the micro-trench gaps (roughness). Numerical results indicate that this insensitiveness is due to the limitation on how much the streamlines can bend into the micro-trenches under these non-Stokes flow ($Re > 10$) conditions, where most of the trenches are partially wetted. Under these conditions the streamlines separate at the edge of the land regions and deflect into the wetted micro-trenches by a finite and almost constant distance, much smaller than the height of the trenches.

These two observations were further corroborated by performing frictional tests on microchannels with fully wetted micro-trenches throughout the whole range of *Re*. As expected, the frictional values remained relatively constant through the range, but more importantly, the friction of the fully wetted microchannels was lower than that of the initially de-wetted microchannels in the lower *Re* region (2–10), suggesting that the fully wetted conditions are more efficient in achieving friction reduction than de-wetted ones. It should be noted that even under these fully wetted conditions, a substantial friction reduction (in the order of 15–18%) is achieved for this non-optimized microgeometry. This is not surprising considering that under these non-Stokes flow conditions the inertia of the flow prevents substantial deflection of the streamlines into the microgeometry. As such, the flow still experiences a more mobile "interface" from the imbibed but stagnant water filling the microgeometry than it would from a solid wall. In other words, for highly inertial conditions, microtextured superhydrophobic surfaces in the Wenzel state can still result in substantial friction reduction, even outperforming the Cassie state. This is extremely important in the design of microtextured friction reduction surfaces, as the geometrical constraints imposed by the Laplace pressure to support air pockets are not present in the Wenzel state.

The work presented here by no means represents a final or universal statement on the effects that pressure and partial wetting of the roughness have on the friction reduction characteristics of microchannel flow. The work is based on a microchannel with water flowing over a transverse groove type microtexture. This may not necessarily be the most efficient friction reduction geometry, and the reasons why the frictional characteristics of the de-wetted microchannels are so high may be specific to this transverse microtexture configuration. Further and more in-depth investigations, including velocity mapping at the interface using μ-PIV, need to (and will) be put in place to validate some

of observations made here. Nevertheless, the findings presented in this paper should be thought provoking and allude to the fact that more emphasis and efforts should be directed towards partial wetting effects and truly understanding the physics behind friction reduction in superhydrophobic microtextured surface flows.

VI. ADDENDUM – ADDITIONAL DISCUSSIONS

A. Stability issues during initial wetting

During the initial wetting phase, a fraction of the shallowest micro-trench elements ($c = 30\ \mu$m) were flooded with water. One possibility for this premature wetting may be addressed to the instability of the Cassie-Baxter state. It is therefore necessary to understand the stability criteria between the two states and the transition conditions from one state to the other. Lafuma and Qu[52] have shown that roughness factor affects the stability of the superhydrophobic criterion. Depending on the surface microgeometry, a critical contact angle θ_c can be found by equating the Wenzel equation and the Cassie-Baxter equation,

$$\cos\theta_c = \frac{(\phi_s - 1)}{(r - \phi_s)}, \tag{4}$$

where the solid fraction ϕ_S and the roughness factor r have been defined in the previous section. According to Eq. (4), three possible regimes are suggested - the Wenzel regime, the stable Cassie-Baxter regime, and the metastable Cassie-Baxter regime. However, even if the contact angle is less than the critical contact angle, studies have shown that the liquid will not necessarily be in the Wenzel regime, but can also be in the metastable Cassie-Baxter state. The droplet in the metastable regime still experiences a 'fakir on a bed of nails' situation but may immediately transition to the Wenzel state if a disturbance is applied.

Conversely, Eq. (4) can be interpreted in terms of the cricitical roughenss factor r_c.[53] If the Wenzel equation and the Cassie-Baxter equation are defined in terms of the Young's contact angle θ_Y, we can again equate the two equations but instead isolate the roughness factor r_c,

$$r_c = \phi_S - \frac{1 - \phi_S}{\cos\theta_Y}. \tag{5}$$

According to this equation, if the actual roughness factor is greater than the critical roughness factor r_c, the liquid will be more energetically stable in the Cassie-Baxter regime. Table II shows the critical roughness factor, solid fraction (assuming an ideal Cassie-Baxter state) and actual effective roughness, $r = 1 + 2c/(a + b)$, for the micro-trench geometries employed in this study. Since the material used in the experiment is PDMS, the contact angle is assumed to be between 110° and 115°.[54] Applying these contact angles will give a range of critical roughness factors. It is noticeable from this table that the shallow depth trenches ($c = 30\ \mu$m and $60\ \mu$m) are less likely to be

TABLE II. Comparison of the solid fraction ϕ_S, estimated critical roughness factor r_c, and the actual roughness factor r_{actual} for different micro-trench configurations used in this study. When calculating the r_c, the contact angle is assumed to be between $\theta_Y = 110°$–115°, hence the range of critical roughness values. The range in contact angle is attributed by the fact that pristine condition microchannels were used rather than microchannels with silanized walls.

Trench dimension	ϕ_S	r_c	r_{actual}
$a = 15\ \mu$m, $c = 30\ \mu$m	0.19	2.1–2.6	1.66
$a = 15\ \mu$m, $c = 60\ \mu$m	0.19	2.1–2.6	2.45
$a = 15\ \mu$m, $c = 120\ \mu$m	0.19	2.1–2.6	3.92
$a = 15\ \mu$m, $c = 230\ \mu$m	0.19	2.1–2.6	6.94
$a = 55\ \mu$m, $c = 30\ \mu$m	0.45	1.8–2.1	1.45
$a = 55\ \mu$m, $c = 60\ \mu$m	0.45	1.8–2.1	1.98
$a = 55\ \mu$m, $c = 120\ \mu$m	0.45	1.8–2.1	2.98
$a = 55\ \mu$m, $c = 230\ \mu$m	0.45	1.8–2.1	4.99

TABLE III. The ratio of prematurely wetted trenches to the total number of trenches for both left and right side trenches combined. Since $a = 15\ \mu$m, $b = 65\ \mu$m, $c = 30\ \mu$m configuration is well below the critical roughness factor, the number of prematurely wetted trenches is the greatest.

Trench dimension (μm) Land × gap × depth	Premature wetting ratio of individual trials (%)				
$a = 15\ \mu$m, $b = 65\ \mu$m, $c = 30\ \mu$m	15	46	36	10	22
$a = 55\ \mu$m, $b = 65\ \mu$m, $c = 30\ \mu$m	0	2	2	0	2

energetically stable in the Cassie-Baxter state and are therefore expected to flood under lower inlet pressures conditions.

As explained in Eq. (5), the liquid will be in an energetically stable Cassie state if the local roughness is greater than the critical roughness factor. This is most likely true for $c = 60\ \mu$m, 120 μm, and 230 μm micro-trench depth channels. However, the roughness factors for both $a = 15\ \mu$m, $c = 30\ \mu$m and $a = 55\ \mu$m, $c = 30\ \mu$m trenches were lower than the critical roughness factor, particularly the $a = 15\ \mu$m, $c = 30\ \mu$m configuration. This indicates that two of the shallowest micro-trench configurations are in a metastable Cassie-Baxter state. The Cassie-Baxter state will fail if it is exposed to disturbance, which was the case when the microchannels were first primed with water. Table III represents the ratio of the number of premature wetting trenches to the total number of trenches of the two shallowest micro-trench microchannels. Since the $a = 15\ \mu$m, $b = 65\ \mu$m, $c = 30\ \mu$m micro-trench channel has the lowest critical roughness factor, the ratio of prematurely wetted trenches was the greatest. Because premature wetting is undesirable, the results suggest that micro-trench depths should also be considered when designing superhydrophobic surfaces in an internal flow.

Since Eqs. (4) and (5) neglects pressure effects, the actual critical roughness is likely to be different. However, the equations will provide a first degree approximation on predicting the stability of the air-water interface.

B. Gas diffusivity in PDMS channels

During the wetting experiment, results indicated that the penetration distances were similar regardless of the micro-trench gap (Fig. 13). This suggests that the air is removed through the PDMS walls with increased pressure instead of compressing the air pockets to resist flooding of the trenches. While studies indicate that PDMS is inherently gas diffusible,[55] thus making it an ideal material for Bio-MEMS application, it may be detrimental for applications in superhydrophobic surfaces. This is especially true for partial two phase flows over isolated cavities filled with air, and the notion of the

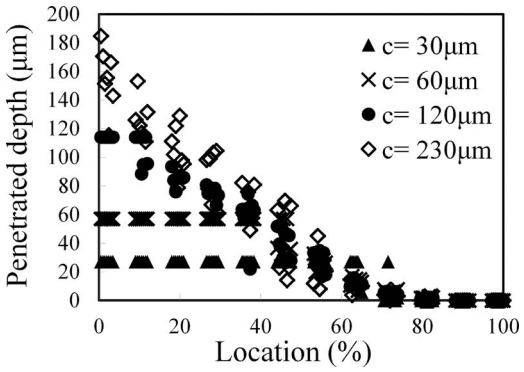

FIG. 13. Absolute values of penetration depth ($a = 15\ \mu$m) as a function of location at $\Delta P = 4000$ Pa (Re $\sim$ 15) for a single microchannel sample. For each repeating trials, the slopes are similar regardless of different micro-trench depths. This suggests that the magnitude of penetration is similar regardless of the micro-trench depth.

air layer acting as a 'cushion' will no longer be valid. Unless special treatment is applied to prevent the gas from permeating through the walls, PDMS may not be an appropriate material to be used as a superhydrophobic surface with isolated gas cavities.

ACKNOWLEDGMENTS

This work was funded by The University of Texas at Austin start-up funds and The University of Texas System STARS (Science and Technology Acquisition and Retention) funds. The authors would like to thank Ravitej Kanapuram and Arnav Chhabra for developing MATLAB code that facilitated the processing of the interface penetration data.

[1] L. Feng, S. Li, Y. Li, H. Li, L. Zhang, J. Zhai, Y. Song, B. Liu, L. Jiang, and D. Zhu, "Super-hydrophobic surfaces: From natural to artificial," Adv. Mater. **14**(24), 1857–1860 (2002).
[2] M. Ma and R. M. Hill, "Superhydrophobic surfaces," Curr. Opin. Colloid Interface Sci. **11**(4), 193–202 (2006).
[3] A. B. D. Cassie and S. Baxter, "Wettability of porous surfaces," Trans. Faraday Soc. **40**, 546–551 (1944).
[4] T. Onda, S. Shibuichi, N. Satoh, and K. Tsujii, "Super-water-repellent fractal surfaces," Langmuir **12**(9), 2125–2127 (1996).
[5] A. Tuteja, W. Choi, J. M. Mabry, G. H. McKinley, and R. E. Cohen, "Robust omniphobic surfaces," Proc. Natl. Acad. Sci. U.S.A. **105**(47), 18200 (2008).
[6] C. H. Choi, U. Ulmanella, J. Kim, C. M. Ho, and C. J. Kim, "Effective slip and friction reduction in nanograted superhydrophobic microchannels," Phys. Fluids **18**(8), 087105 (2006).
[7] A. V. Belyaev and O. I. Vinogradova, "Effective slip in pressure-driven flow past super-hydrophobic stripes," J. Fluid Mech. **652**, 489–499 (2010).
[8] C. Lee and C. J. Kim, "Maximizing the giant liquid slip on superhydrophobic microstructures by nanostructuring their sidewalls," Langmuir **25**(21), 12812–12818 (2009).
[9] D. Byun and H. C. Park, "Drag reduction on micro-structured super-hydrophobic surface," in *Proceedings of the 2006 IEEE International Conference on Robotics and Biomimetics* (IEEE, Kunming, 2006), pp. 818–823.
[10] P. Joseph, C. Cottin-Bizonne, J. M. Benoit, C. Ybert, C. Journet, P. Tabeling, and L. Bocquet, "Slippage of water past superhydrophobic carbon nanotube forests in microchannels," Phys. Rev. Lett. **97**(15), 156104 (2006).
[11] C. H. Choi and C. J. Kim, "Large slip of aqueous liquid flow over a nanoengineered superhydrophobic surface," Phys. Rev. Lett. **96**(6), 66001 (2006).
[12] J. P. Rothstein, "Slip on superhydrophobic surfaces," Annu. Rev. Fluid Mech. **42**, 89–109 (2010).
[13] N. V. Priezjev, A. A. Darhuber, and S. M. Troian, "Slip behavior in liquid films on surfaces of patterned wettability: Comparison between continuum and molecular dynamics simulations," Phys. Rev. E **71**(4), 041608 (2005).
[14] E. Lauga and H. A. Stone, "Effective slip in pressure-driven Stokes flow," J. Fluid Mech. **489**(1), 55–77 (2003).
[15] L. Bocquet and J. L. Barrat, "Flow boundary conditions from nano-to micro-scales," Soft Matter **3**(6), 685–693 (2007).
[16] J. R. Philip, "Flows satisfying mixed no-slip and no-shear conditions," Z. Angew. Math. Phys. **23**(3), 353–372 (1972).
[17] R. Pit, H. Hervet, and L. Léger, "Friction and slip of a simple liquid at a solid surface," Tribol. Lett. **7**(2), 147–152 (1999).
[18] J. Ou and J. P. Rothstein, "Direct velocity measurements of the flow past drag-reducing ultrahydrophobic surfaces," Phys. Fluids **17**(10), 103606 (2005).
[19] D. C. Tretheway and C. D. Meinhart, "Apparent fluid slip at hydrophobic microchannel walls," Phys. Fluids **14**, L9–L12 (2002).
[20] D. C. Tretheway and C. D. Meinhart, "A generating mechanism for apparent fluid slip in hydrophobic microchannels," Phys. Fluids **16**, 1509–1515 (2004).
[21] H. Udagawa, "Drag reduction of Newtonian fluid in a circular pipe with a highly water-repellent wall," J. Fluid Mech. **381**, 225–238 (1999).
[22] C. F. Carlborg, G. Stemme, and W. V. D. Wijngaart, "Microchannels with substantial friction reduction at large pressure and large flow," in *Proceedings of the 22nd IEEE International Conference on Micro Electro Mechanical Systems* (IEEE, Sorrento, 2009), pp. 39–42.
[23] M. Jin, X. Feng, J. Xi, J. Zhai, K. Cho, L. Feng, and L. Jiang, "Super Hydrophobic PDMS Surface with Ultra Low Adhesive Force," Macromol. Rapid Commun. **26**(22), 1805–1809 (2005).
[24] L. Bocquet and E. Lauga, "A smooth future?," Nat. Mater. **10**(5), 334–337 (2011).
[25] J. Ou, B. Perot, and J. P. Rothstein, "Laminar drag reduction in microchannels using ultrahydrophobic surfaces," Phys. Fluids **16**(12), 4635–4643 (2004).
[26] R. N. Wenzel, "Resistance of solid surfaces to wetting by water," Ind. Eng. Chem. **28**(8), 988–994 (1936).
[27] C. Lee and C. J. Kim, "Underwater restoration and retention of gases on superhydrophobic surfaces for drag reduction," Phys. Rev. Lett. **106**(1), 14502 (2011).
[28] C. F. Carlborg, M. Do-Quang, G. Stemme, G. Amberg, and W. V. D. Wijngaart, "Continuous flow switching by pneumatic actuation of the air lubrication layer on superhydrophobic microchannel walls," in *Proceedings of the 21st IEEE International Conference on Micro Electro Mechanical Systems* (IEEE, Tucson, 2008), pp. 599–602.
[29] T. N. Krupenkin, J. A. Taylor, E. N. Wang, P. Kolodner, M. Hodes, and T. R. Salamon, "Reversible wetting-dewetting transitions on electrically tunable superhydrophobic nanostructured surfaces," Langmuir **23**(18), 9128–9133 (2007).
[30] P. Muralidhar, N. Ferrer, R. Daniello, and J. P. Rothstein, "Influence of slip on the flow past superhydrophobic circular cylinders," J. Fluid Mech. **1**(1), 1–18 (2011).

[31] C. Henoch, T. Krupenkin, P. Kolodner, J. Taylor, M. Hodes, A. Lyons, C. Peguero, and K. Breuer, "Turbulent drag reduction using superhydrophobic surfaces," AIAA Paper No. 2006-3192, 2006.
[32] R. J. Daniello, N. E. Waterhouse, and J. P. Rothstein, "Drag reduction in turbulent flows over superhydrophobic surfaces," Phys. Fluids **21**, 085103 (2009).
[33] C. Neinhuis and W. Barthlott, "Characterization and distribution of water-repellent, self-cleaning plant surfaces," Ann. Bot. (London) **79**(6), 667 (1997).
[34] P. G. De Gennes, F. Brochard-Wyart, and D. Quéré, *Capillarity and Wetting Phenomena: Drops, Bubbles, Pearls, Waves* (Springer, New York, 2004), pp. 215–219.
[35] D. Qu, A. Lafuma, and J. Bico, "Slippy and sticky microtextured solids," Nanotechnology **14**, 1109 (2003).
[36] Y. C. Jung and B. Bhushan, "Biomimetic structures for fluid drag reduction in laminar and turbulent flows," J. Phys.: Condens. Matter **22**, 035104 (2010).
[37] C. H. Choi, K. J. A. Westin, and K. S. Breuer, "Apparent slip flows in hydrophilic and hydrophobic microchannels," Phys. Fluids **15**, 2897–2902 (2003).
[38] E. Lauga and M. P. Brenner, "Dynamic mechanisms for apparent slip on hydrophobic surfaces," Phys. Rev. E **70**(2), 026311 (2004).
[39] C. Cottin-Bizonne, C. Barentin, E. Charlaix, L. Bocquet, and J. L. Barrat, "Dynamics of simple liquids at heterogeneous surfaces: Molecular-dynamics simulations and hydrodynamic description," Eur. Phys. J. E **15**(4), 427–438 (2004).
[40] D. Byun, J. Kim, H. S. Ko, and H. C. Park, "Direct measurement of slip flows in superhydrophobic microchannels with transverse grooves," Phys. Fluids **20**(11), 113601 (2008).
[41] H. Lorenz, M. Despont, N. Fahrni, J. Brugger, P. Vettiger, and P. Renaud, "High-aspect-ratio, ultrathick, negative-tone near-UV photoresist and its applications for MEMS," Sens. Actuators, A **64**(1), 33–39 (1998).
[42] S. Natarajan, D. Chang-Yen, and B. Gale, "Large-area, high-aspect-ratio SU-8 molds for the fabrication of PDMS microfluidic devices," J. Micromech. Microeng. **18**, 045021 (2008).
[43] I. Papautsky, T. Ameel, and A. B. Frazier, "A review of laminar single-phase flow in microchannels," in *Proceedings of the 2001 ASME International Mechanical Engineering Congress and Exposition* (ASME, New York, 2001), pp. 1–9.
[44] C. Cottin-Bizonne, A. Steinberger, B. Cross, O. Raccurt, and E. Charlaix, "Nanohydrodynamics: The intrinsic flow boundary condition on smooth surfaces," Langmuir **24**(4), 1165–1172 (2008).
[45] C. Cottin-Bizonne, C. Barentin, and L. Bocquet, "Scaling laws for slippage on superhydrophobic fractal surfaces," Phys. Fluids **24**(1), 012001 (2012).
[46] R. K. Shah and A. L. London, *Laminar Flow Forced Convection in Ducts: A Source Book for Compact Heat Exchanger Analytical Data* (Academic, New York, 1978), pp. 256–259.
[47] J. Hyväluoma and J. Harting, "Slip flow over structured surfaces with entrapped microbubbles," Phys. Rev. Lett. **100**(24), 246001 (2008).
[48] A. Steinberger, C. Cottin-Bizonne, P. Kleimann, and E. Charlaix, "High friction on a bubble mattress," Nat. Mater. **6**(9), 665–668 (2007).
[49] C. Ybert, C. Barentin, C. Cottin-Bizonne, P. Joseph, and L. Bocquet, "Achieving large slip with superhydrophobic surfaces: Scaling laws for generic geometries," Phys. Fluids **19**, 123601 (2007).
[50] R. Clift, J. R. Grace, and M. E. Weber, *Bubbles, Drops, and Particles* (Academic, New York, 1978), pp. 38–41.
[51] T. Gervais, J. El-Ali, A. Günther, and K. F. Jensen, "Flow-induced deformation of shallow microfluidic channels," Lab Chip **6**(4), 500–507 (2006).
[52] A. Lafuma and D. Qu, "Superhydrophobic states," Nat. Mater. **2**(7), 457–460 (2003).
[53] T. J. Kim and C. H. Hidrovo, "Stability analysis of Cassie-Baxter State under pressure driven flow," in *Proceedings of the 8th International Conference on Nanochannels, Microchannels, and Minichannels collocated with 3rd Joint US-European Fluids Engineering* (ASME, Montreal, 2010), pp. 1657–1662.
[54] A. Mata, A. J. Fleischman, and S. Roy, "Characterization of polydimethylsiloxane (PDMS) properties for biomedical micro/nanosystems," Biomed. Microdevices **7**(4), 281–293 (2005).
[55] Z. Cui, *Nanofabrication: Principles, Capabilities and Limits* (Springer, Berlin, 2008), pp. 203–205.